Improved reconstructions and generalized filtered back projection for optical projection tomography

Udo Jochen Birk,[1,2,*] Alex Darrell,[3,4] Nikos Konstantinides,[5] Ana Sarasa-Renedo,[5] and Jorge Ripoll[1]

[1]Institute of Electronic Structure & Laser, Foundation for Research and Technology-Hellas, FORTH, P.O Box 1527, 71110 Heraklion, Greece

[2]Kirchhoff Institut für Physik, Universität Heidelberg, INF 227, 69120 Heidelberg, Germany

[3]Institute of Computer Science, FORTH, 71110 Heraklion, Greece

[4]Currently at Medical Vision Laboratory, Department of Engineering Science, Oxford University, Parks Road, Oxford OX1 3PJ, UK

[5]Institute of Molecular Biology and Biotechnology, FORTH, 71110 Heraklion, Greece

*Corresponding author: uspoeri@kip.uni-heidelberg.de

Received 10 June 2010; revised 27 November 2010; accepted 13 December 2010; posted 14 December 2010 (Doc. ID 129829); published 26 January 2011

Optical projection tomography (OPT) is a noninvasive imaging technique that enables imaging of small specimens (<1 cm), such as organs or animals in early developmental stages. In this paper, we present a set of computational methods that can be applied to the acquired data sets in order to correct for (a) unknown background or illumination intensity distributions over the field of view, (b) intensity spikes in single CCD pixels (so-called "hot pixels"), and (c) refractive index mismatch between the media in which the specimens are embedded and the environment. We have tested these correction methods using a variety of samples and present results obtained from *Parhyale hawaiensis* embedded in glycerol and in sea water. Successful reconstructions of fluorescence and absorption OPT images have been obtained for weakly scattering specimens embedded in media with nonmatched refractive index, thus advancing OPT toward routine *in vivo* imaging.

OCIS codes: 100.6950, 170.6960, 110.3010, 170.3010.

1. Introduction

Optical projection tomography (OPT) is a valuable tool for *in vivo* studies of small specimens, typically smaller than 1 cm in size [1–5]. It can close the gap between diffraction-limited imaging, such as confocal laser scanning microscopy, and the various macroscale imaging techniques used in medical imaging, such as diffuse optical tomography [6,7], magnetic resonance imaging [8], and many others, providing good optical resolution at a reasonable imaging/penetration depth. In its original form, OPT was limited to transparent samples, but computational methods also have been derived for low-scattering samples [9,10] as well as for turbid media [11]. It is presently the only tool to address questions related to both morphological structures and molecular imaging in a single instrument due to its unique ability to combine three-dimensional (3D) images of anatomy (by means of absorption contrast) with the specificity of molecular imaging (by means of fluorescence labeling), which can also be correlated with fluorescence lifetime imaging [12]. Furthermore, considerable effort has been put into the development of advanced image reconstruction procedures in order to enhance the 3D resolution achievable [13,14]. However, for many of the specific problems arising when imaging live samples, the presently available

0003-6935/11/040392-07$15.00/0

reconstruction methods for OPT data are not sufficient.

In particular for *in vivo* imaging, a compromise regarding the optical properties of the embedding medium and its influence on the survival of the specimens has to be made. Most often, the natural environment of the specimens is unsuitable for imaging because of refractive index mismatch at the optical boundaries, resulting in a high degree of image degradation. Additional mechanical instabilities of the instrument or the specimen's holder might add to the blurring of the 3D reconstructions. In this work, we present improvements of the reconstruction methods, which allow correcting for image blur due to refractive index mismatch of the embedding media with respect to the surrounding container. Furthermore, we present a set of tools aimed at quantitative imaging, such as estimation of the illumination intensity distribution by Zernike polynomials decomposition and removal of nonlinear effects of the CCD response.

This paper is structured as follows: in Section 1, we present the setup of the present OPT instrumentation, followed by a short description of the measurement procedure in Section 2. Section 3 explains the image reconstruction process, giving details on the improvements of the postacquisition data evaluation methods, in particular the routines for capillary detection, estimating illumination intensity, removal of "hot pixels" (i.e., intensity spikes in the acquired images), and correction of refractive index mismatch of the embedding medium. In Section 4, we discuss our findings and present our conclusions.

2. Setup

The present OPT setup, together with the coordinate system, is depicted in Fig. 1. As described in detail [1–3], for OPT, the samples can be imaged either in transmission mode or in fluorescence excitation mode. For both white light transmission and fluorescence imaging, super bright LEDs have been implemented, allowing homogeneous illumination of

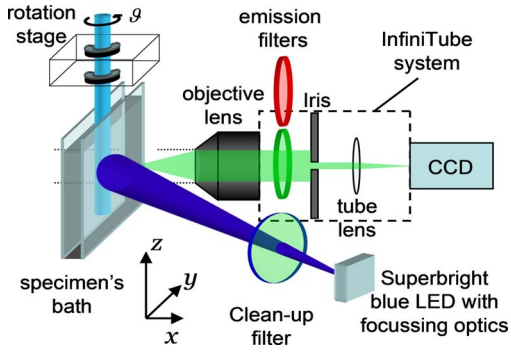

Fig. 1. (Color online) OPT setup for fluorescence imaging. Small specimens are mounted in a glass capillary, which is attached to a rotation stage. Excitation is performed in quasi-epifluorescence mode, with the light source placed in close proximity to the objective lens. Detection optics (objective lens, filters, iris diaphragm, tube lens, and CCD camera) are connected by an InfiniTube system mounted directly to the optical breadboard.

larger samples, such as dissected mouse organs (typical dimensions would be up to 2.0 cm in length and 0.5 cm in diameter). In fluorescence mode, a blue 5 W LED (Luxeon V Star, Philips Lumileds Lighting, San Jose, California) is mounted on the same side as the detection objective lens, thus approximating an epifluorescence illumination. For morphological (absorption) imaging, a super bright 5 W white LED (Luxeon V Star, Philips Lumileds Lighting) is placed together with an optical diffuser onaxis to operate in transmission mode. For both operation modes, a custom-made far field light microscope (based on the InfiniTube system, Infinity Photo-Optical, Boulder, Colorado) is used in combination with a range of long-working-distance objective lenses (Mitutoyo Corp., Kanagawa, Japan) with magnifications of 20×, 10×, and 5×. For larger specimens (i.e., lower magnification), corrected achromat lenses are used for imaging (LSB08-A, Thorlabs, Newton, New Jersey). A highly sensitive electron-multiplying (EM)-CCD camera (Ixon DV885, 14 bit, Andor Technology, Belfast, Northern Ireland) acquires the two-dimensional (2D; projection) images for different views under various rotation angles. A rotation stage (8MR180, Standa, Vilnius, Lithuania, 36,000 steps per revolution) is employed to actuate the samples with steps of typically $\vartheta = 0.72°$, resulting in a total of 500 images for one data set.

Two methods for mounting the specimens are available. Smaller specimens (e.g., *Caenorhabditis elegans, Drosophila melanogaster, Parhyale hawaiensis*) are mounted in a disposable glass capillary (Blaubrand–intraMARK, BRAND, Wertheim, Germany), which is placed in a bath of glycerol with a refractive index matching that of the glass capillary walls. The imaging windows of the bath consist of borosilicate microscopy cover slips, again with the same refractive index. The mounting device, attached to two manual translation stages (G065040000, LINOS Photonics, Göttingen, Germany) at the top and bottom of the rotation stage, holds the glass capillaries and allows precise adjustment of the tilt and the center of rotation. For larger specimens, the lower manual translation stage is replaced by a magnet. In this case, the specimens are simply glued to a metallic piece that can easily be attached to the magnet, which also facilitates alignment with the rotation axis. In its present state, the magnet holder does not allow alignment of the tilt; this needs to be adjusted prior to the measurement while gluing the metal part to the specimens.

3. Measurements

Various embedding media (e.g., glycerol, halocarbon oil, sea water, methyl cellulose, phosphate-buffered saline, a mixture of benzyl alcohol and benzyl benzoate [1]) for both small and larger samples have been tested and shown to allow imaging with the OPT setup, although with varying degrees of image degradation due to refractive index mismatch. While optimal imaging can be done by embedding the specimens in

glycerol, many of the animals cannot be kept alive in this environment, and a different approach has been taken to correct for this refractive index mismatch, as described in Section 4.D.

Measurements are carried out either in transmission (absorption) mode or in fluorescence excitation mode. Gain and integration time of the EM-CCD camera are set to make use of the full dynamic range of the camera while minimizing overall acquisition time, readout noise (Gaussian distributed), and Poisson noise (photon shot and EM-CCD gain). Typical values are a gain of 70 (110) and an integration time of 0.2 s (4 s) for transmission (fluorescence) imaging.

For imaging of *P. hawaiensis*, no fix was applied, since fixation procedures resulted in an increase of background autofluorescence. To eliminate movement, the specimens were incubated in 40 mM sodium azide for 1 h prior to the experiment, and then transferred to a viscous mounting medium consisting of 4% methyl cellulose in sea water.

4. Image Reconstruction

Several improvements to the image reconstruction process have been implemented in the Matlab (The MathWorks Inc., Natick, Massachusetts) programming environment, correcting for a multitude of factors that determine the quality of the final reconstructions. All of these correction methods are designed to operate on the fully acquired 3D data stack. As shown in [13], precise correction of the nonlinearity of the CCD pixels and normalization of the illumination intensity (light output fluctuations) are crucial for OPT. Here, we present additional methods to estimate the background intensity for nonhomogeneous illumination as obtained for specimens mounted in capillaries and to correct for refractive index mismatch of the embedding medium. Both methods are essential for quantitative imaging with the OPT setup. These methods include automated detection of the glass capillary walls, segmentation of the projection images, and Zernike polynomial decomposition of the background intensity after removal of so-called "hot pixels."

A. Capillary Detection

The specimens have to be rotated and, thus, have to be fixed to the rotation stage. In order to meet this requirement, smaller samples are mounted in microcapillaries, which are particularly suitable for *in vivo* experiments of, for example, *P. hawaiensis*, *C. elegans*, *Tribolium castaneum*, or *D. melanogaster*, because the movement of the animals is severely restricted [15], and a suitable microenvironment can be chosen by selecting a specific embedding medium (e.g., with an added anesthetic). The refractive index of the immersion medium of the OPT specimen's bath is matched to that of the glass capillaries and windows and, whenever possible, an embedding medium with the same refractive index is chosen. Despite the refractive index matching for one particular wavelength, different dispersion of the different materials results in the capillary walls still being visible in the projection images [see Fig. 2(a)], and it is often useful to know their location and orientation. For instance, the determination of the background intensities (see Section 4.B) relies on separation (segmentation) of the image area into objects, capillaries (walls), and remaining background area inside/outside the glass capillaries. Additionally, movement of the capillary walls might indicate positioning errors and drifts in the stages used [15]. To automatically detect the capillary walls, we implemented a forward radon transform of the acquired images, where the straight lines of the capillary walls appear as single points, the (y, φ) positions of which contain the information on the position and tilt angle of the respective capillary wall in the image data.

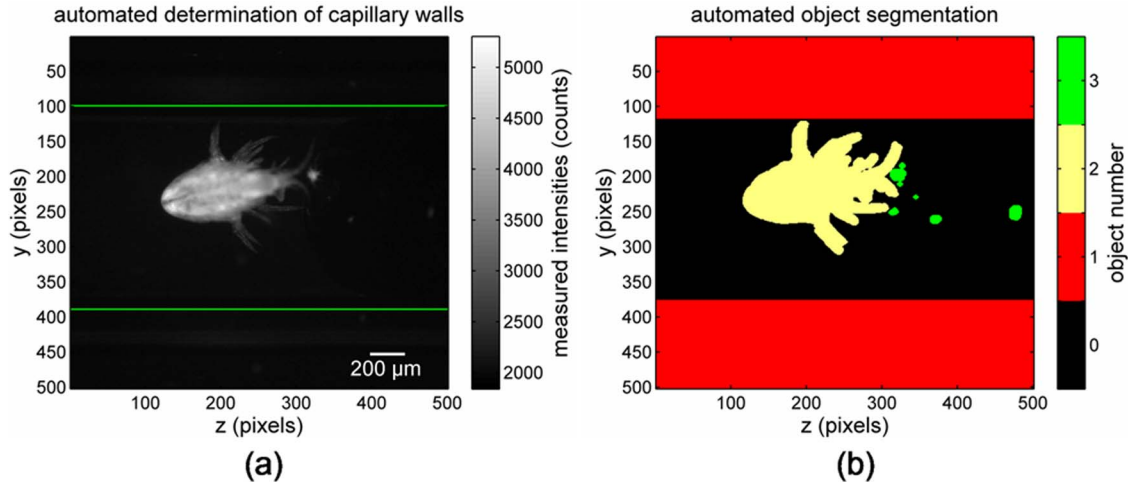

Fig. 2. (Color online) (a) 2D projections (raw image data) can be used to automatically determine the positions of the capillary walls (horizontal lines) by means of a forward radon transform. b) Automated object segmentation algorithm is implemented to separate the image area into the background (object number 0), specimens (2), area outside the capillary (1, including the glass walls), and sometimes additional fragments (3, e.g., residues from the culture media).

B. Background Estimation

The LED light cone cannot be fully collimated, which results in an (only) approximate Gaussian illumination in our present setup. To correct for this nonuniformity, it is essential that a correct prediction of the background intensities is made in order to avoid bowl artifacts [13] in the reconstructions. Generally, this should be done by measuring the illumination (background) after removing the objects, but with the capillaries in place. However, after removing the specimens, an exact repositioning of the empty capillaries is virtually impossible. Therefore, a method to estimate the background in the acquired 2D projection image is implemented. For this purpose, objects need to be segmented, and the intensities of the remaining image area are used to fit the background data.

1. *Object Segmentation*

Two methods for automated object segmentation are implemented by using either border detection via an edge detection filter (Sobel gradient filter) or thresholding. The thresholding algorithm works best for uniformly illuminated samples. However, since at this point of the evaluation the illumination intensity distribution (background) might not be known, the edge detection method often provides more reliable results in terms of proper segmentation of the object area. Figure 2 shows the result of the automated segmentation procedure for an experiment with *P. hawaiensis*, a crustacean, which was embedded in glycerol. In order to reduce the computation time, full field images (1004×1002 pixels) are resized to a quarter of their size prior to evaluation.

For both segmentation methods, a combination of erode and dilate functions is applied to the segmented images. For the edge detection algorithm dilating is necessary to join all pixels surrounding the object, before this outline can be filled. For the thresholding algorithm, erode/dilate is used to eliminate individual high intensity pixels from the resulting segmentation. The algorithm has been optimized for the following background fit, thus slightly overestimating the specimen's area.

2. *Background Fit*

If measured background data (dark field) is not available, the background signal can be estimated after object segmentation and capillary detection to correct for nonuniform illumination. In case of fluorescence image data, the background signal is higher than the dark-field values due to bleed-through of the laser (or LED) excitation light. Acquiring a flatfield image would solve this problem, but does not account for the influence of the capillaries (the specimens can only be removed together with the capillaries). When putting back the empty capillary inside the microscope after removal of the specimens, the capillaries are never in exactly the same position as before. For both transmitted white light and fluorescence data, refraction at the capillary walls results in a nonuniform illumination. Hence, the background signal needs to be estimated for the acquired projection data. For background estimation, a nonlinear least squares fit for Zernike polynomial [16] decomposition has been implemented to obtain piston, tilt, and defocus (and, if required, higher-order corrections) from the intensity values corresponding

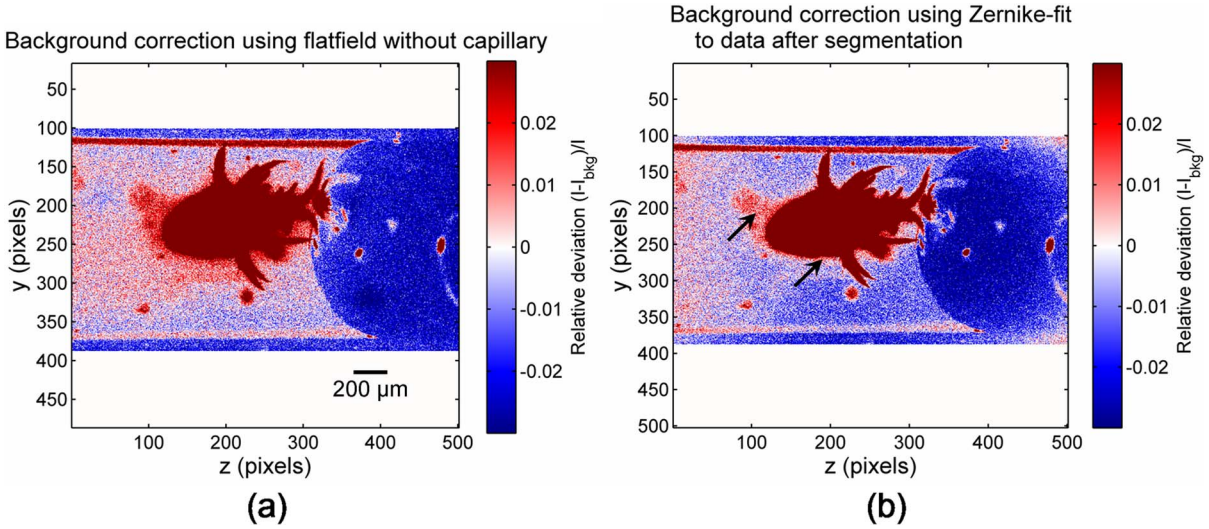

Fig. 3. (Color online) Comparison of background correction using measured flatfield data and background estimation from 2D projection data. Depicted are the deviations of the measured intensity I after subtraction of the background data I_{bkg}, normalized to the measured intensities. (a) Measured flatfield data without the capillary has been used as background data. (b) Zernike fit has been applied to each of the 2D projection images after segmentation to determine the background intensities once the images were acquired. It can be seen that the capillaries also affect the illumination intensities: the flatfield-corrected data is brighter along the center of the capillary ($y = 250$), i.e., at the pixels surrounding the object. Zernike decomposition can be used to overcome this problem. Arrows point at areas where the improvements are most pronounced.

Table 1. Coefficients $c_{n,m}$ of the Zernike Polynomial Decomposition (First Three Orders) on the Cartesian Unit Interval $[-1;1]$ Obtained from a Nonlinear Least Squares Fit to the Background Intensities of the 2D Projection Images after Segmentation[a]

Name	Piston	Tilt z	Tilt y	Defocus	Astigm.1	Astigm.2
Order	$n=0$	$n=1$	$n=1$	$n=2$	$n=2$	$n=2$
	$m=0$	$m=0$	$m=1$	$m=1$	$m=2$	$m=0$
$Z_{n,m}(z,y)$	1	z	y	$2(z^2+y^2)-1$	z^2-y^2	$2zy$
$c_{n,m}$	2012.11	−8.20	3.77	−48.97	29.17	−1.13

[a]These results are used to estimate the illumination intensity at each pixel.

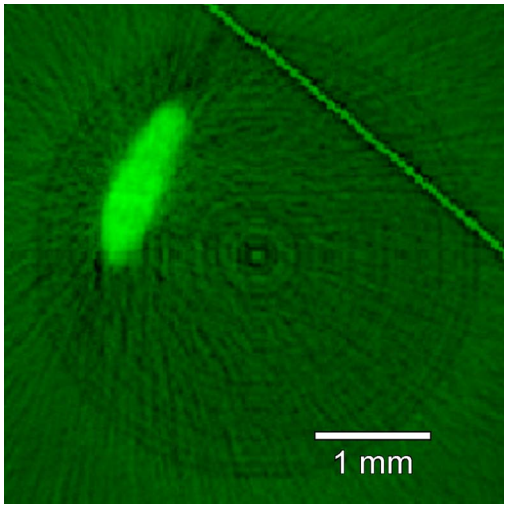

Fig. 4. (Color online) So-called hot pixels of the EM-CCD camera, where the intensity in a single pixel is suddenly boosted because of electronic noise during the EM gain stage, appear as line artifacts (top right) in the reconstructed images. Nonlinear response of the individual CCD pixels appear as concentric rings in the reconstructions, as shown by Walls *et al.* [13].

to pixels outside the object but inside the capillary. Although Zernike functions $Z_{n,m}(z,y)$ are most often used in wavefront measurements [17] (i.e., to represent the phase of the electromagnetic field), they are generally suitable for describing any arbitrary surface: in our case, the intensities over the CCD array.

In Fig. 3, the conventional background correction method using an acquired flatfield image [Fig. 3(a)] is compared to that of the Zernike decomposition $B(z,y)=\sum c_{n,m}Z_{n,m}(z,y)$ of the background intensities $B(z,y)$ obtained from the 2D projection images [Fig. 3(b)]. The second approach has an additional advantage in that it can also be applied to measurements in which the capillary axis is not concentric with the rotation axis. The resulting coefficients $c_{n,m}$ of the Zernike polynomial decomposition (on the Cartesian unit area, interval $[-1;1]$) using the first three orders are shown in Table 1.

C. Removal of Hot Pixels

As is characteristic for the EM-CCD, the acquired images sometimes show intensity spikes in a single pixel. Often these spike values also affect neighboring pixels due to an overflow of the electronic well. Setting a maximum value for the meaningful data intensities can be used to detect these hot pixels. On average, hot pixels occur in only one out of 500 projection images, but, when left untreated, they result in line artifacts in the reconstructed images (see Fig. 4). In order to remove these false data values, a

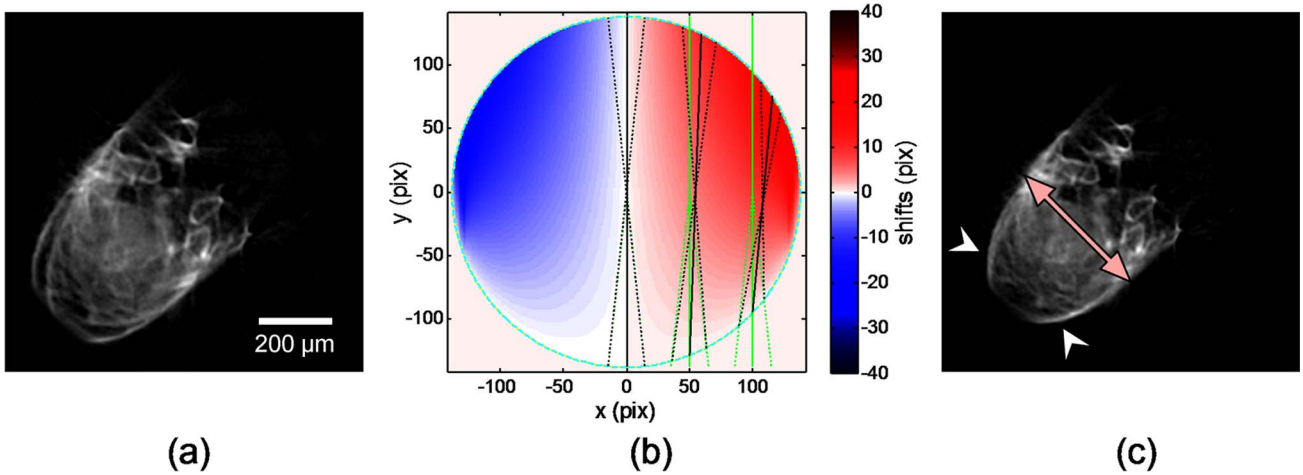

Fig. 5. (Color online) (a) Standard filtered back-projection reconstruction along the parallel (green) lines in (b). (b) Cross section through the capillary with radius $R=137.8$ pixels (cyan). As embedding medium, sea water with 4% methyl cellulose is used. Because of the lower index of refraction ($n=1.344$), the acquired projections are no longer parallel to the optical axis (apart from the central ray at $x=0$). The geometrical focus points are shown for light rays focused inside the capillary ($y=0$) at positions $x=0,50,100$. The dotted bright green lines depict the apparent focus positions at 0.7 NA, whereas the true focal positions within the capillary are shown in black. (c) Result of the reconstruction along the true lines of projection [black lines in (b)]. Arrowheads indicate where reconstruction artifacts have been removed, and the arrow indicates that the overall magnification in the reconstruction has been corrected.

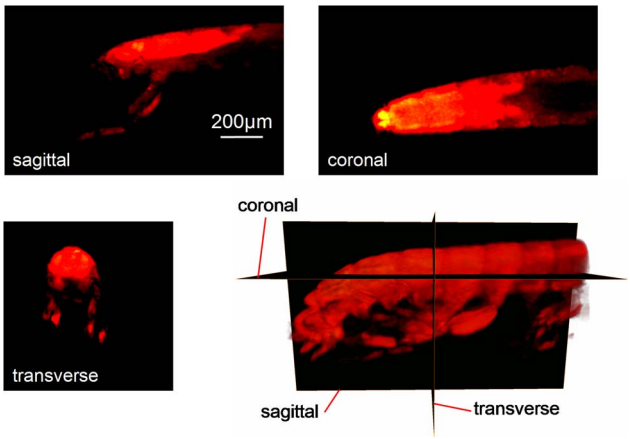

Fig. 6. (Color online) *P. hawaiensis* tail with muscle-specific labeling with dsRed, 40 mM sodium-azide for 1 h, no fixation, embedded in sea water with 4% methyl cellulose. Sagittal, coronal, and transverse cross sections obtained from the 3D reconstruction of the acquired 2D OPT projections. Bottom right: View of the 3D volume rendering (Media 1, which additionally shows the anatomy of the other half of the animal reconstructed from the white light data).

9×9 region of interest (ROI) around the central pixel with maximum intensity is chosen, and all intensity values within the ROI are replaced by the median of the ROI.

D. Correction of Refractive Index Mismatch

Especially in case of *in vivo* experiments, only a limited choice of suitable embedding media is available in which the specimens can survive. However, microscope objective lenses are designed to work with embedding of a specific refractive index only. The use of media with different refractive indices results in serious image degradation due to optical aberrations. The effect becomes even more pronounced for objects extended along the optical axis, as in the case of OPT. Generally, for OPT, objective lenses with low numerical aperture (NA, typically around 0.2) are used in order to have a large depth of field and, thus, be able to have the whole sample in focus and to obtain projection images. For low NA imaging, it is often sufficient to use paraxial approximations or even geometrical optics, and, with the exception of spherical aberration, all higher-order aberrations can be neglected. In this case, the acquired images are no longer orthogonal projections of the 3D object. Knowing the refractive index of the embedding media (and of all the glass interfaced within the sample volume), we can calculate the geometrical focus within the whole depth of field, even in the case of refractive index mismatch [see Fig. 5(b)]. This information can then be used to back project the acquired 2D images along the "true" lines of projection. Figure 5 shows an example of a slice through reconstructed absorption data (white light measurement) of a sample of *P. hawaiensis* that was embedded in sea water with 4% methyl cellulose (Sigma-Aldrich Co, cat. no. M0387). Because of spherical aberrations, the standard back-projection approach is unable to yield reconstructions of this object [see Fig. 5(a)]. By back projecting the acquired 2D images along the calculated trajectories, we can reconstruct the 3D object [see Fig. 5(c)].

The reconstruction procedure for a 2D slice (size $N \times N$) to be reconstructed from data acquired on a single line of the CCD chip is as follows: first, a Hann filter is applied to the acquired projection data on the full frequency spectrum, yielding the filtered data set d. For each rotation angle ϑ, we calculate the shift matrix $s_{k,l}(\vartheta)$ [Fig. 5(b)] of each voxel with x coordinate k and y-coordinate $l(-N/2 \le k, l \le N/2)$. We then calculate the index of the pixel on the CCD line, which needs to be back projected (i.e., contributes to this voxel):

$$t_{k,l} = k \cos\vartheta + l \sin\vartheta + s_{k,l}(\vartheta). \quad (1)$$

In our reconstruction approach, we use a linear interpolation between neighboring data points of the acquired projection data d. Hence, the reconstructed intensity $I_{k,l}$ in voxel (k,l) is a linear combination of the two neighboring CCD pixels d^- and d^+, corresponding to $\mathrm{floor}(t_{k,l})$ and $\mathrm{ceil}(t_{k,l})$:

$$I_{k,l} = (t_{k,l} - \mathrm{floor}(t_{k,l}))d^+ + (\mathrm{ceil}(t_{k,l}) - t_{k,l})d^-. \quad (2)$$

As in the conventional inverse radon transform, the final image I is the sum of $I_{k,l}$ over all angles ϑ.

5. Results and Conclusions

We have applied the enhanced OPT technique to image specimens in the range of several tens of micrometers up to about 1 cm. Figure 6 depicts the reconstruction of *P. hawaiensis* with muscle-specific expression of DsRed fluorescent protein [18]. As a preliminary step toward *in vivo* experiments, this animal was imaged in a solution of 4% methyl cellulose in sea water.

Using geometrical optics, we are able to generalize the concept of OPT to nonorthogonal projections. In theory, this method can be applied to any form of projection, be it parallel, diverging, or anything else, as long as we either know the trajectory along which the projections are taken or are able to calculate it. Note that, although by limiting the number of projections to 180°, standard filtered back projections would get rid of the double reconstruction [in Fig. 5(a)], but several artifacts would still be visible in the images. First, the scale of the reconstruction would be wrong, as can be seen by comparing the lateral extent (size) of the reconstructions in Figs. 5(a) and 5(c). Second, since the result of spherical aberrations can be looked at as a varying center of rotation (not only varying over time, but also different for each reconstructed voxel x,y), object structures in the reconstructions would appear blurred, and, furthermore, streak artifacts would be noticeable. Using the presented modified back projection, these limitations can be overcome, and quantitative imaging in terms

of signal amplitude and positions (size) within the 3D reconstructions is now possible also for arbitrary embedding.

The authors wish to acknowledge support from the European Commission (grants MEIF-CT-2006-041827 and FP7 grant 201792 "FMT-XCT") and the Bill and Melinda Gates Foundation. Special thanks to M. Averof for his help with the *P. hawaiensis* specimens.

References

1. J. Sharpe, U. Ahlgren, P. Perry, B. Hill, A. Ross, J. Hecksher-Sorensen, R. Baldock, and D. Davidson, "Optical projection tomography as a tool for 3D microscopy and gene expression studies," Science **296**, 541–545 (2002).
2. J. Sharpe, "Optical projection tomography," Annu. Rev. Biomed. Eng. **6**, 209–228 (2004).
3. M. J. Boot, C. H. Westerberg, J. Sanz-Ezquerro, J. Cotterell, R. Schweitzer, M. Torres, and J. Sharpe, "In vitro whole-organ imaging: 4D quantification of growing mouse limb buds," Nat. Method **5**, 609–612 (2008).
4. A. Darrell, H. Meyer, K. Marias, M. Brady, and J. Ripoll, "Weighted filtered backprojection for quantitative fluorescence optical projection tomography," Phys. Med. Biol. **53**, 3863–3881 (2008).
5. C. Vinegoni, L. Fexon, P. F. Feruglio, M. Pivovarov, J. Figueiredo, M. Nahrendorf, A. Pozzo, A. Sbarbati, and R. Weissleder, "High throughput transmission optical projection tomography using low cost graphics processing unit," Opt. Express **17**, 22320–22332 (2009).
6. R. B. Schulz, J. Ripoll, and V. Ntziachristos, "Noncontact optical tomography of turbid media," Opt. Lett. **28**, 1701–1703 (2003).
7. A. Sarasa-Renedo, R. Favicchio, U. Birk, G. Zacharakis, C. Mamalaki, and J. Ripoll, "Source intensity profile in noncontact optical tomography," Opt. Lett. **35**, 34–36 (2010).
8. P. C. Lauterbur, "Magnetic resonance zeugmatography," Pure Appl. Chem. **40**, 149–157 (1974).
9. C. Vinegoni, C. Pitsouli, D. Razansky, N. Perrimon, and V. Ntziachristos, "In vivo imaging of Drosophila melanogaster pupae with mesoscopic fluorescence tomography," Nat. Method **5**, 45–47 (2008).
10. C. Vinegoni, D. Razansky, J. Figueiredo, M. Nahrendorf, V. Ntziachristos, and R. Weissleder, "Normalized Born ratio for fluorescence optical projection tomography," Opt. Lett. **34**, 319–321 (2009).
11. F. Vasefi, E. Ng, B. Kaminska, G. H. Chapman, K. Jordan, and J. J. L. Carson, "Transmission and fluorescence angular domain optical projection tomography of turbid media," Appl. Opt. **48**, 6448–6457 (2009).
12. J. McGinty, K. B. Tahir, R. Laine, C. B. Talbot, C. Dunsby, M. A. A. Neil, L. Quintana, J. Swoger, J. Sharpe, and P. M. W. French, "Fluorescence lifetime optical projection tomography," J. Biophotonics **1**, 390–394 (2008).
13. J. R. Walls, J. G. Sled, J. Sharpe, and R. M. Henkelman, "Correction of artefacts in optical projection tomography," Phys. Med. Biol. **50**, 4645–4665 (2005).
14. A. Darrell, J. Swoger, L. Quintana, J. Sharpe, K. Marias, M. Brady, and J. Ripoll, "Improved fluorescence optical projection tomography reconstruction," SPIE Newsroom 1–4 (2008).
15. U. J. Birk, M. Rieckher, N. Konstantinides, A. Darrell, A. Sarasa-Renedo, H. Meyer, N. Tavernarakis, and J. Ripoll, "Correction for specimen movement and rotation errors for in-vivo optical projection tomography," Biomed. Opt. Express **1**, 87–96 (2010).
16. M. Born and E. Wolf, *Principles in Optics* (Wheaton, 1983).
17. J. R. Fienup, J. C. Marron, T. J. Schulz, and J. H. Seldin, "Hubble space telescope characterized by using phase-retrieval algorithms," Appl. Opt. **32**, 1747–1767 (1993).
18. A. Pavlopoulos and M. Averof, "Establishing genetic transformation for comparative developmental studies in the crustacean *Parhyale hawaiensis*," Proc. Natl. Acad. Sci. USA **102**, 7888–7893 (2005).